Chapter 5

Geometry of structures of enstrophy and dissipation fields in decaying homogeneous isotropic turbulence

5.1 DNS database

The numerical database used here is that of Horiuti & Fujisawa (2008), henceforth referred to as HF. It corresponds to a DNS of incompressible homogeneous isotropic turbulence decaying in time in a cubic domain of side length 2π, with periodic boundary conditions. We use runs corresponding to 256^3, 512^3, and 1024^3 grid points with the same value of the kinematic viscosity, ν, resulting in a similar Taylor-microscale Reynolds number, $Re_\lambda \approx 77$, and in grid resolution criteria, $k_{\max}\bar{\eta}$, of approximately 1, 2, and 4, respectively. Together with the fact that the initial conditions are the same for the three runs, they can be used to compare the geometry of flow structures at different resolutions. Additional parameters for each run at the instant of maximum enstrophy are shown in Table 5.1, extracted from HF, where more details of the computational method can be obtained. The three velocity fields at this time instant for the three grid resolutions are the database for the present study.

In this chapter, we apply the methodology proposed in Chapter 2 for the study of the geometry of structures in turbulence to the enstrophy and dissipation fields. Local enstrophy is defined as

N	ν	Re_λ	$\langle K \rangle$	$\langle \epsilon \rangle$	L	λ	$\bar{\eta}(\times 10^{-3})$	$k_{\max}\bar{\eta}$
256^3	0.00138	77.20	0.900	0.654	0.469	0.138	8.00	1.02
512^3	0.00138	76.87	0.897	0.654	0.469	0.137	8.00	2.05
1024^3	0.00138	77.43	0.904	0.654	0.468	0.138	8.00	4.09

Table 5.1: Parameters for the computed cases: grid points, N; kinematic viscosity, ν; Taylor-microscale Reynolds number, Re_λ; average kinetic energy, $\langle K \rangle$; average dissipation rate, $\langle \epsilon \rangle$; integral length scale, L; Taylor microscale, λ; average Kolmogorov length scale, $\bar{\eta}$; grid resolution criterion, $k_{\max}\bar{\eta}$ (where $k_{\max}$ is the largest dynamically significant wavenumber). From HF

$\omega_i\omega_i$, while local dissipation is defined as $\epsilon \equiv 2\,\nu S_{ij}S_{ij}$. S_{ij} is the strain-rate tensor and ω_i is the vorticity field, which is related to the rotation-rate tensor, Ω_{ij}, by $\Omega_{ij} = -\epsilon_{ijk}\,\omega_k/2$, ϵ_{ijk} being the Levi-Civita symbol. Thus: $\omega_i\omega_i = 2\,\Omega_{ij}\Omega_{ij}$. Strain- and rotation-rate tensors are obtained from the velocity gradient tensor, $\partial u_i/\partial x_j$, as:

$$S_{ij} = \frac{1}{2}\left(\frac{\partial u_i}{\partial x_j} + \frac{\partial u_j}{\partial x_i}\right), \qquad \Omega_{ij} = \frac{1}{2}\left(\frac{\partial u_i}{\partial x_j} - \frac{\partial u_j}{\partial x_i}\right). \tag{5.1}$$

We will consider the dissipation rescaled by $(2\,\nu)^{-1}$, that is, $S_{ij}S_{ij}$.

5.2 Multi-scale decomposition

We plot in Figure 5.1 the volume pdfs (left) and the spectra (right), in Fourier space, of the two fields, $\omega_i\omega_i$ and $S_{ij}S_{ij}$, for the three grid resolutions (256^3, 512^3, 1024^3). It can be observed that the pdf of $\omega_i\omega_i$ has longer tails than that of $S_{ij}S_{ij}$. This indicates that large amplitude events in the enstrophy field are more prevalent than in the dissipation field (see Chen et al., 1997), and thus, that $\omega_i\omega_i$ is more intermittent than $S_{ij}S_{ij}$, which is in agreement with results from experiments (Zeff et al., 2003) and numerical simulations (Siggia, 1981; Kerr, 1985; Chen et al., 1997), using the flatness of each field to measure its intermittency. The discrepancy in the spectra of $\omega_i\omega_i$ and $S_{ij}S_{ij}$ increases with the wavenumber, k, that is, for smaller scales. This is also in agreement with the results from numerical simulations at higher Reynolds numbers of Ishihara et al. (2003), who found that the maximum difference between spectra of $\omega_i\omega_i$ and $S_{ij}S_{ij}$ peaks at $k\bar{\eta} \approx 0.4$.

Figure 5.2 shows the effect in physical space of the multi-scale decomposition for $\omega_i\omega_i$ with 512^3

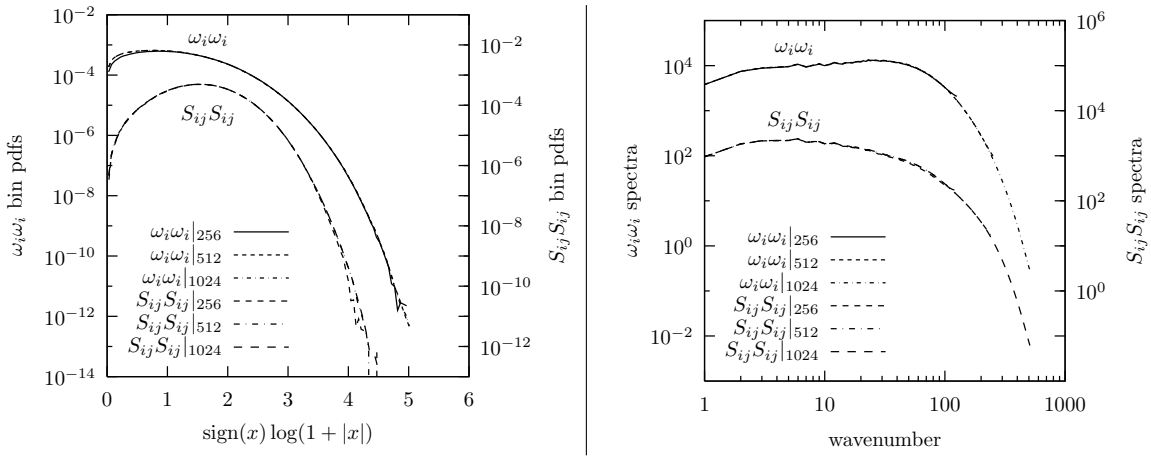

Figure 5.1: Volume pdfs in physical domain (left) and spectra in Fourier domain (right) of $\omega_i\omega_i$ and $S_{ij}S_{ij}$ fields for the three grid resolutions (256^3, 512^3, and 1024^3). Note that the volume pdfs use a transformation of the form $\mathrm{sign}(x)\log(1+|x|)$ in the abscissa coordinate, and that curves for $\omega_i\omega_i$ and $S_{ij}S_{ij}$ fields use two different vertical axes (both in the pdfs and the spectra), shifted one decade for a clear view (non-intersecting curves)

grid points, as an example, through plane cuts in the three principal directions of the cubic domain, compared to the original field (top left).

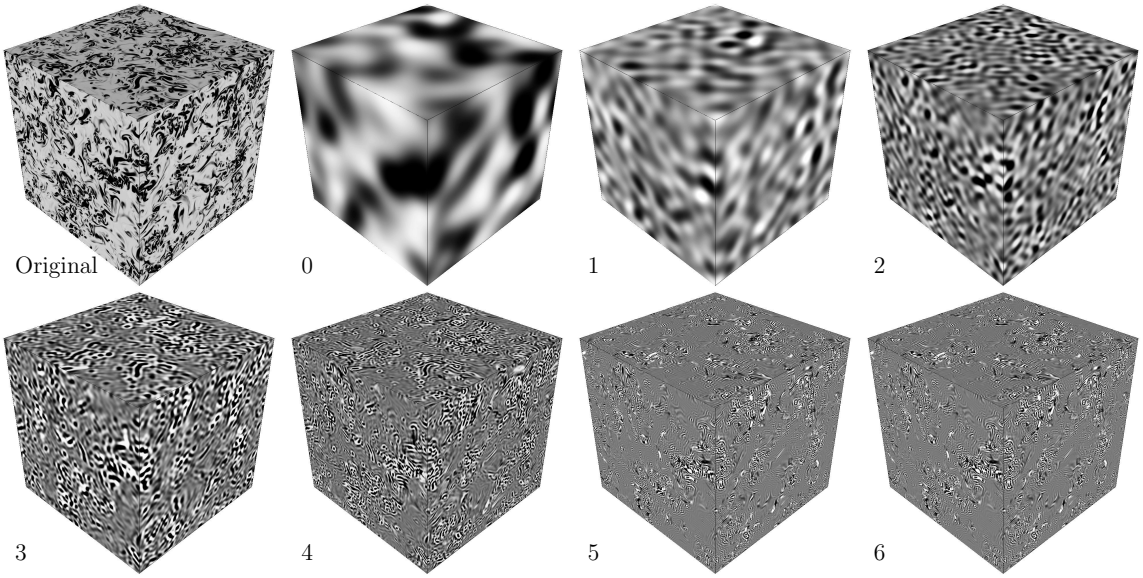

Figure 5.2: Tri-plane cuts of $\omega_i\omega_i$ and its multi-scale component fields for the 512^3 case

Volume pdfs (physical domain) and spectra (Fourier domain) of the original and component fields after the multi-scale decomposition are shown in Figure 5.3, for $\omega_i\omega_i$ (top) and $S_{ij}S_{ij}$ (bottom) fields in the 1024^3 case. Scales are named by scale numbers from 0 to 7. Increasing scale numbers, when

referred to the component fields in which the original field is decomposed, indicate smaller scales. Thus, 0 corresponds to the largest scale, and 1, 2,... correspond to smaller and smaller scales. For the 256^3 and 512^3 cases similar plots (not shown) can be obtained with 5 and 6 as the maximum scale numbers respectively. Note how, for both $\omega_i\omega_i$ and $S_{ij}S_{ij}$, the range of the pdfs increases for

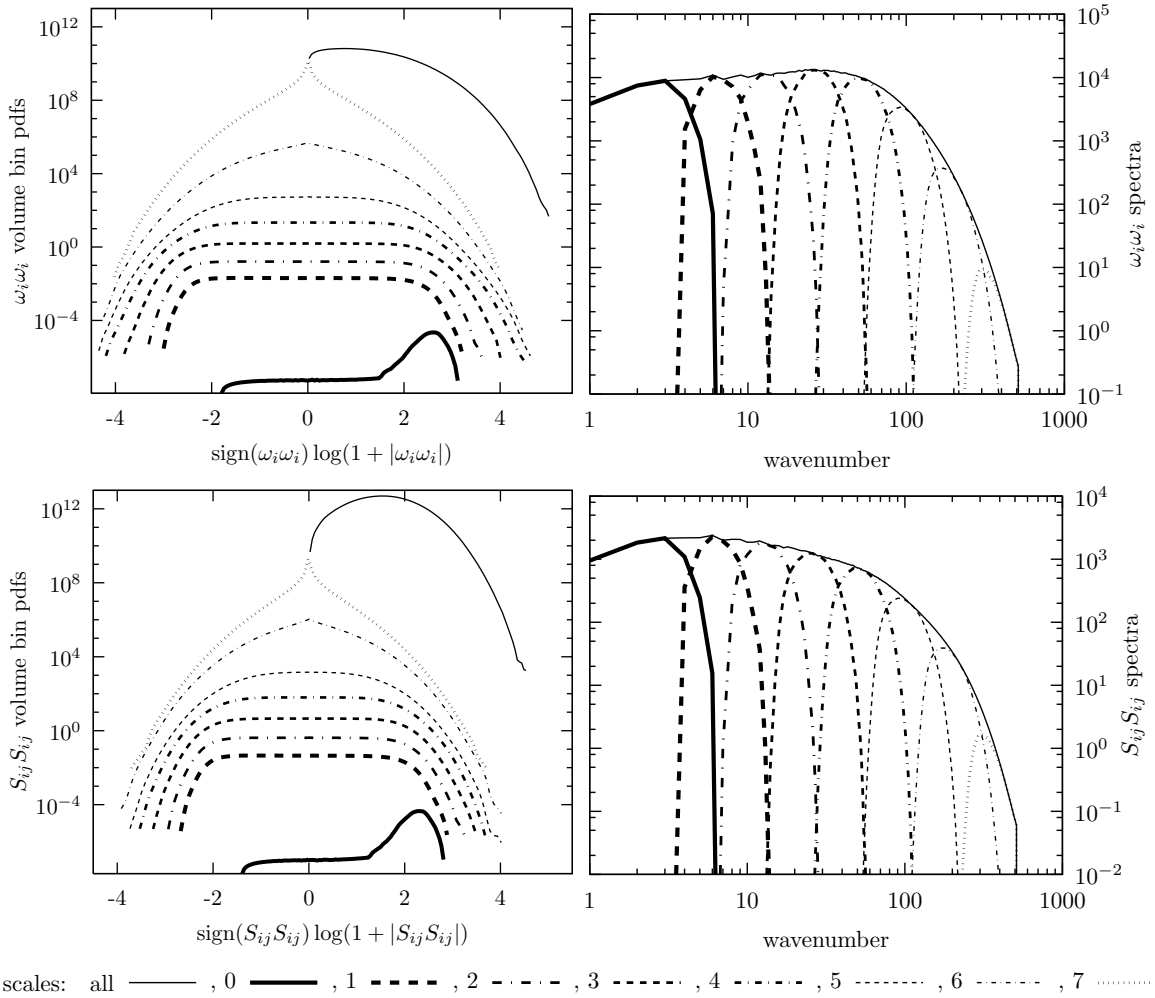

Figure 5.3: Effect of the multi-scale decomposition in the 1024^3 case for $\omega_i\omega_i$ (top) and $S_{ij}S_{ij}$ (bottom) fields on the volume pdfs in physical domain (left) and on the spectra in Fourier domain (right). Note that the volume pdfs have been shifted vertically to accommodate all scales and the original fields in a clearer view. Also, instead of using a log-scale in the abscissa of the pdf plots, since there are negative values for all filtered scales, a transformation of the form $\sign(x)\log(1+|x|)$ is used for each field x

increasing scale number (i.e., smaller scales), indicating that fluctuations of both fields are higher in the small scales, and therefore, that intermittency also increases for those smaller scales. Previous multi-scale studies of turbulence have shown this property (Kennedy & Corrsin, 1961; Meneveau,

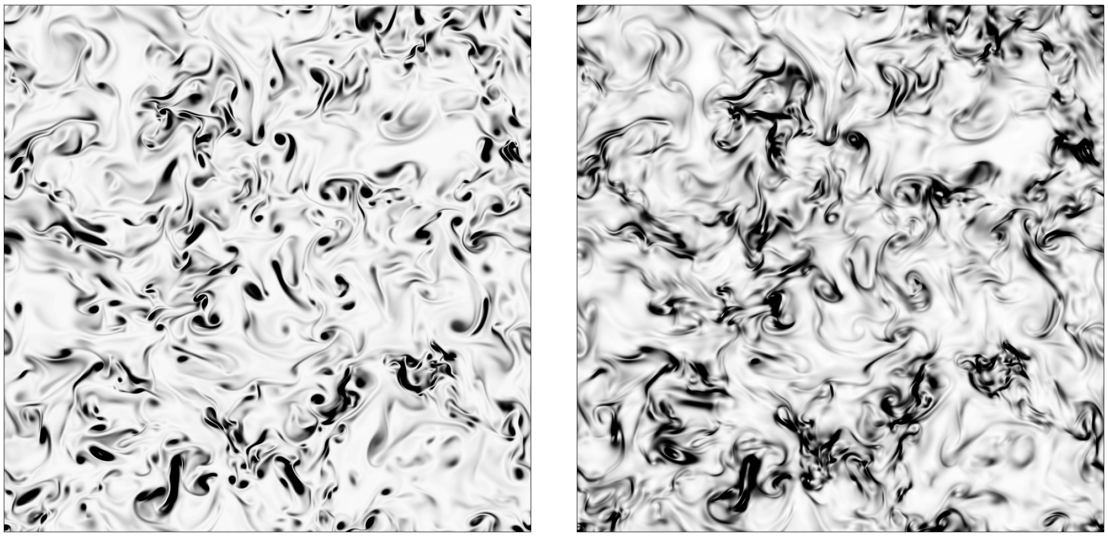

Figure 5.4: Plane cuts of $\omega_i\omega_i$ (left) and $S_{ij}S_{ij}$ (right) normal to one of the principal directions of the cubic domain at half its side length for the 1024^3 case

1991; Brasseur & Wang, 1992; Okamoto et al., 2007).

Figure 5.4 includes plane cuts of $\omega_i\omega_i$ (left) and $S_{ij}S_{ij}$ (right) fields, for the 1024^3, at half the length of the physical domain in one of the principal directions of the cube. Zoomed parts of those plane cuts are shown in Figure 5.5 for the three grid resolutions (256^3, 512^3, and 1024^3, from left to right) for both $\omega_i\omega_i$ (top) and $S_{ij}S_{ij}$ (bottom) fields. It can be observed that, particularly in the 256^3 case, the smallest scales are quite different from the higher-resolution cases. Figure 5.6 shows zoomed parts of the plane cuts corresponding to the component field at scale number 5 for the three grid resolutions, which is the highest scale number attainable in the multi-scale decomposition of the 256^3 case and therefore contains the structures at the smallest scales captured in this flow at that grid resolution. It is clear from the two-dimensional fields that structures educed with the lowest grid resolution, 256^3, can be significantly different from the ones at higher grid resolutions, 512^3 and 1024^3. Intuitively, a geometrical characterization of those structures would be affected by that fact, and its effect would be noticed in the application of the methodology proposed above.

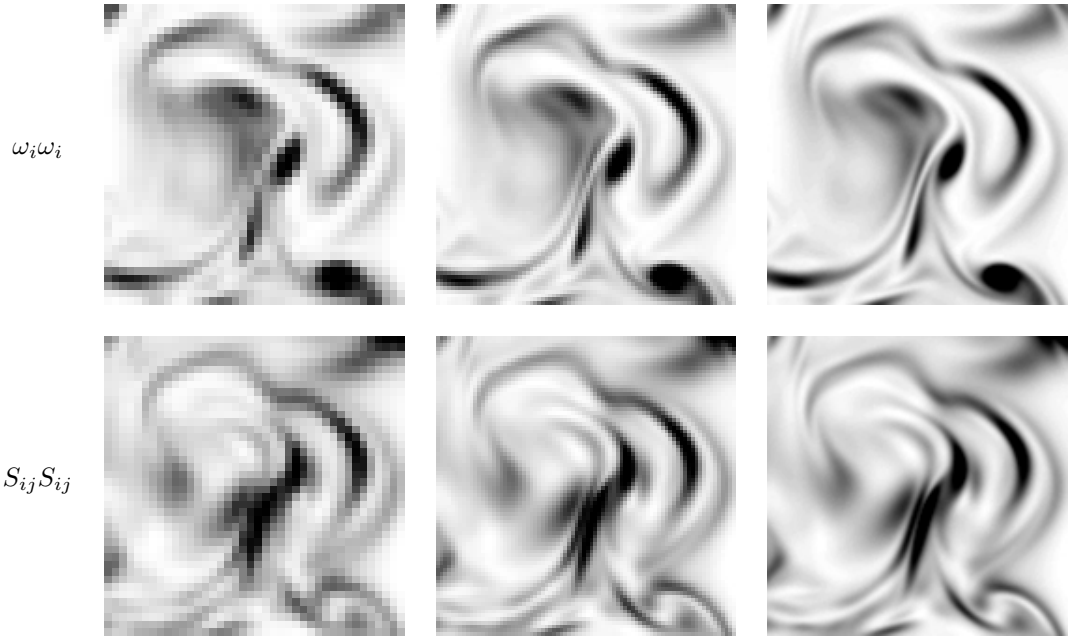

Figure 5.5: Zoomed parts of plane cuts of $\omega_i\omega_i$ (top) and $S_{ij}S_{ij}$ (bottom) in one of the principal directions of the cubic domain at half its side length for the three grid resolutions 256^3 (left), 512^3 (center), and 1024^3 (right). Greyscale has been renormalized to the zoomed region for better clarity

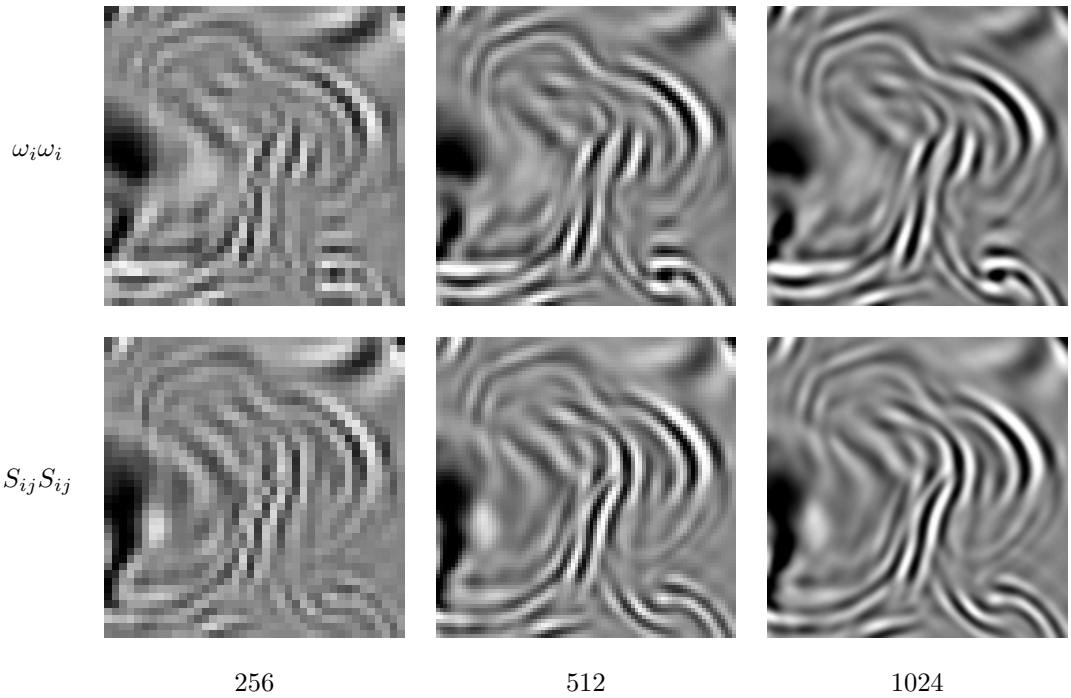

Figure 5.6: Zoomed parts of plane cuts of component field at scale number 5 for $\omega_i\omega_i$ (top) and $S_{ij}S_{ij}$ (bottom) in one of the principal directions of the cubic domain at half its side length for the three grid resolutions 256^3 (left), 512^3 (center), and 1024^3 (right). Greyscale has been renormalized to the zoomed region for better clarity

5.3 Characterization and classification of individual structures

In Figure 5.7 we present the three-dimensional visualization spaces (formed by $\hat{S}, \hat{C}, \lambda$ axes) with the glyphs (simple spheres, in this case) representing each structure after its geometrical characterization. The top row corresponds to $\omega_i\omega_i$ and the bottom row to $S_{ij}S_{ij}$, for increasing grid resolution (256^3, 512^3, and 1024^3) from left to right. The spheres are scaled by the lognormalized area of the corresponding structure. The color of each sphere represents the scale number to which it belongs. As in §4.3, the largest scale is not included in the analysis, for being strongly dependent on the boundary conditions and forcing applied. Neither is the smallest scale (for each grid resolution), to avoid interference between grid resolution effects and the iso-contouring process. The fact that we have three different grid-resolutions for the equivalent field allows us to verify whether that interference occurs. This is discussed at the end of §5.4. Thus, scales 1–4, 1–5 and 1–6 are represented for the 256^3, 512^3, and 1024^3 grid resolutions, respectively. Top views ($(\hat{S}, \hat{C})$-plane) of these visualization spaces are shown in Figure 5.8, where the differences between $\omega_i\omega_i$ and $S_{ij}S_{ij}$ fields can be better realized.

In Figure 5.9 we show the breakdown by increasing scale number (top to bottom) of the three-dimensional visualization spaces for the $\omega_i\omega_i$ field for the three grid resolutions (256^3, 512^3, and 1024^3), increasing from left to right. Top views ($(\hat{S}, \hat{C})$-plane) of each visualization space can be seen in Figure 5.10. Figures 5.11 and 5.12 are the equivalent ones for $S_{ij}S_{ij}$.

We discuss first the case with the highest resolution (1024^3). Structures of both $\omega_i\omega_i$ and $S_{ij}S_{ij}$ fields show a continuous transition of their corresponding glyphs in the visualization space, with varying scale (see right plots of Figures 5.7 and 5.8). Structures at the largest scale of both fields (top-right corner of Figures 5.9 and 5.11) are mainly blob-like; some get closer to the tube-like region with small stretching (high λ). At the smallest scale (bottom right corner of Figures 5.9 and 5.11), dominant structures of both fields are sheet-like (low values of $\hat{C}$ and λ). The intermediate scales present a different behavior for each field: $\omega_i\omega_i$ shows a high concentration of structures near the

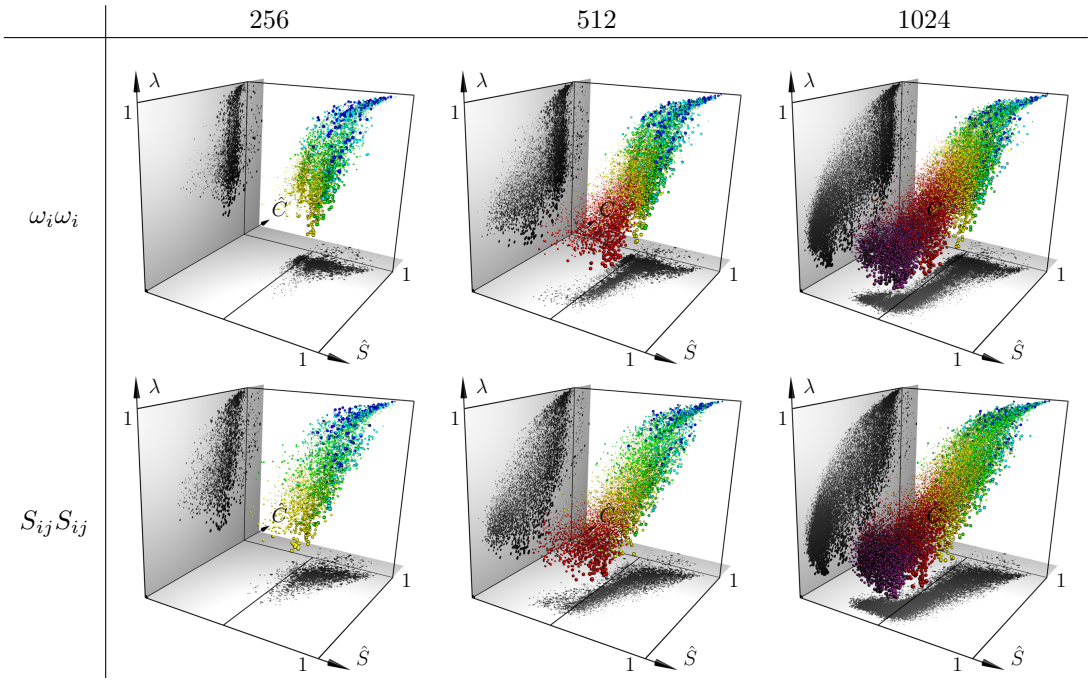

Figure 5.7: 3D views of the visualization spaces, with glyphs (spheres) representing educed structures, colored by scale number (all merged in each visualization space) and scaled by the lognormalized area of the corresponding structure, for $\omega_i\omega_i$ (top row) and $S_{ij}S_{ij}$ (bottom row) at 256^3 (left), 512^3 (center), and 1024^3 (right) grid resolutions

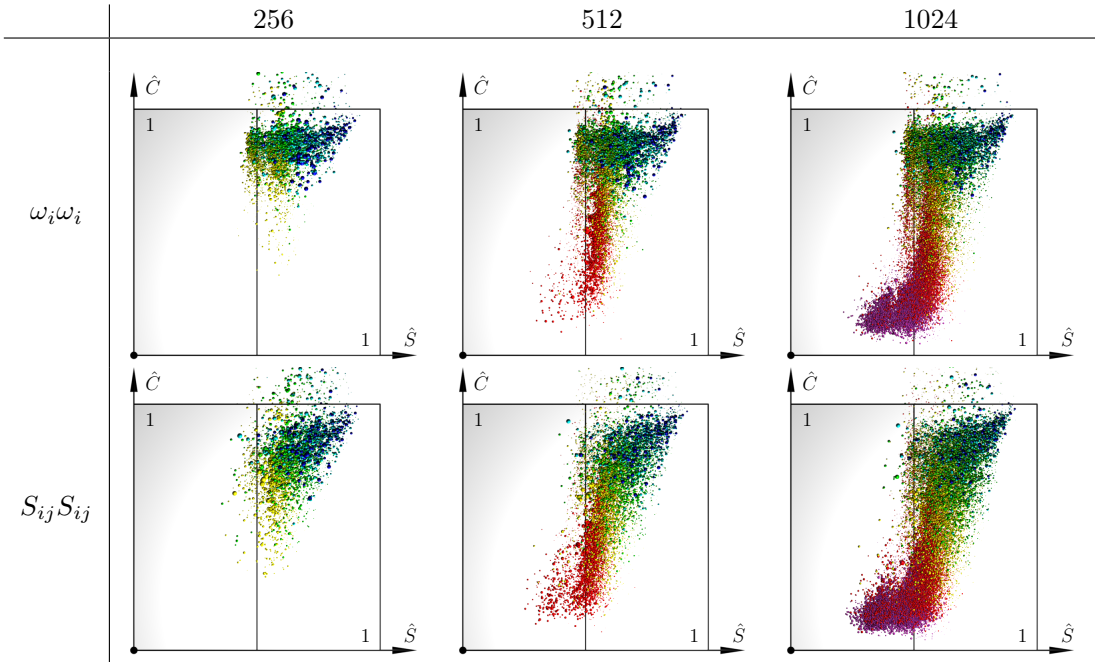

Figure 5.8: Top views ($(\hat{S},\hat{C})$-plane) of the visualization spaces, with glyphs (spheres) representing educed structures, colored by scale number and scaled by the lognormalized area of the corresponding structure, for $\omega_i\omega_i$ (top row) and $S_{ij}S_{ij}$ (bottom row) at 256^3 (left), 512^3 (center), and 1024^3 (right) grid resolutions

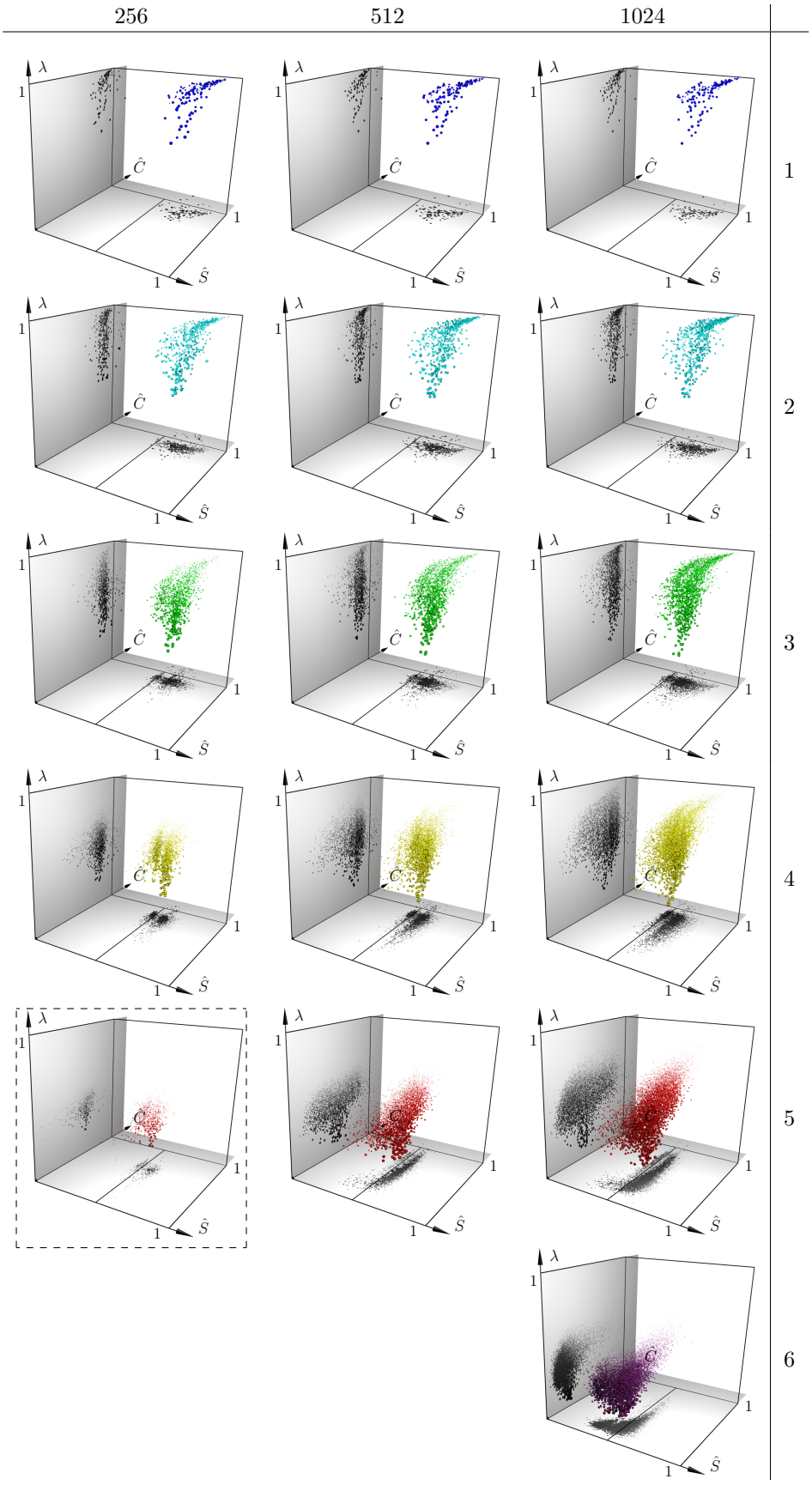

Figure 5.9: Breakdown, by scale number (increasing top to bottom), of 3D views of the visualization spaces for $\omega_i\omega_i$ at 256^3 (left), 512^3 (center), and 1024^3 (right) grid resolutions

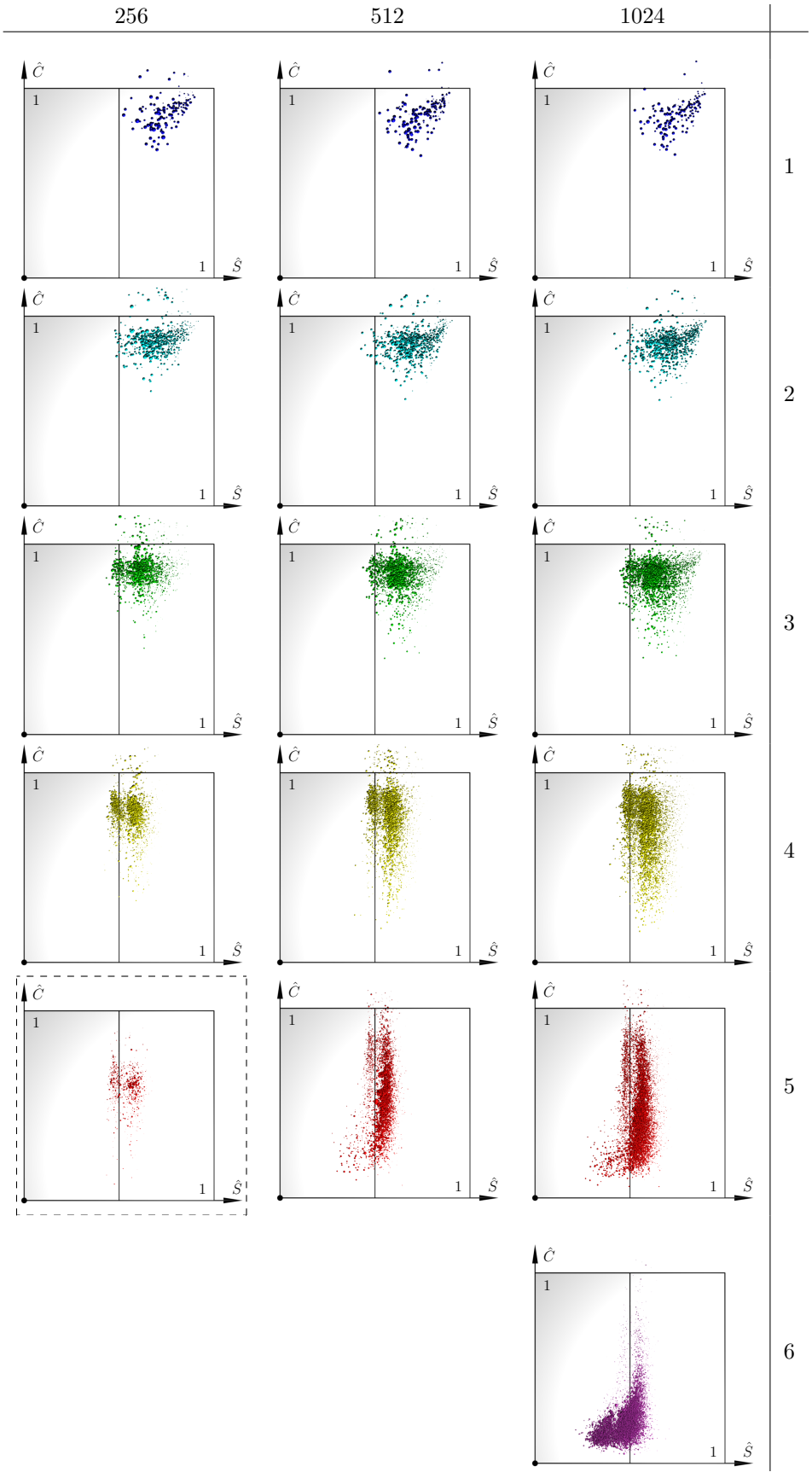

Figure 5.10: Breakdown, by scale number (increasing top to bottom), of top views ($(\hat{S}, \hat{C})$-plane) of the visualization spaces for $\omega_i\omega_i$ at 256^3 (left), 512^3 (center), and 1024^3 (right) grid resolutions

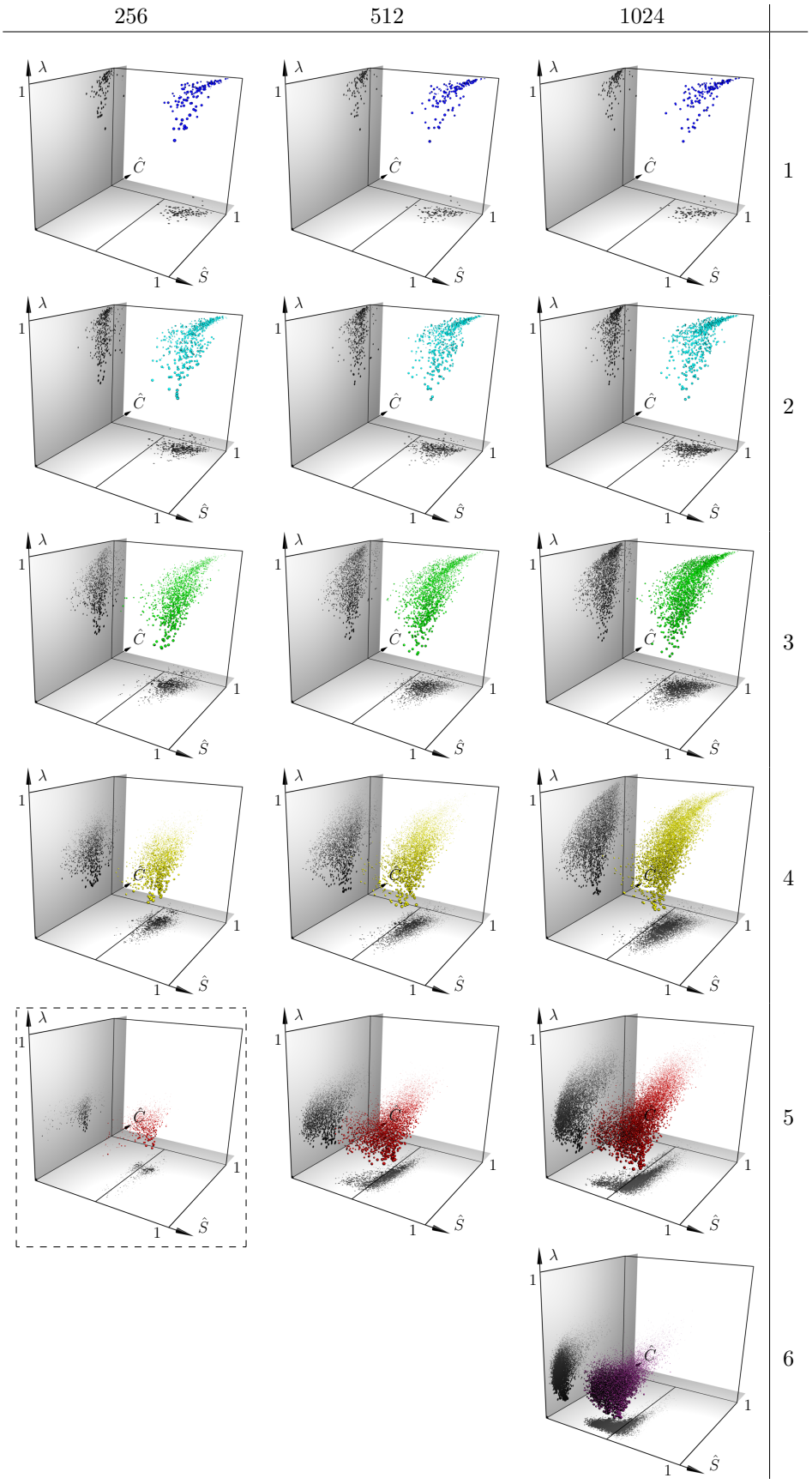

Figure 5.11: Breakdown, by scale number (increasing top to bottom), of 3D views of the visualization spaces for $S_{ij}S_{ij}$ at 256^3 (left), 512^3 (center), and 1024^3 (right) grid resolutions

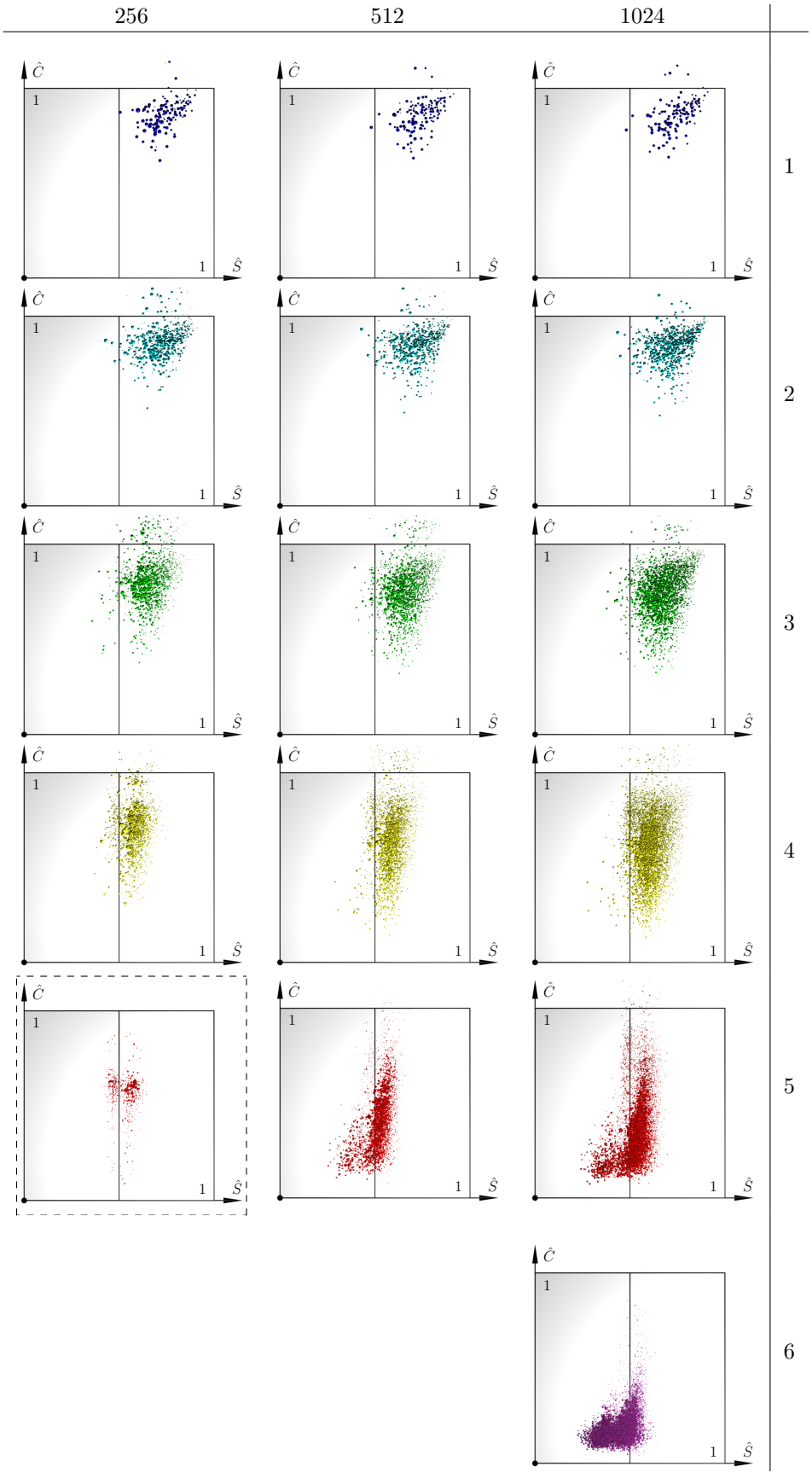

Figure 5.12: Breakdown, by scale number (increasing top to bottom), of top views ($(\hat{S}, \hat{C})$-plane) of the visualization spaces for $S_{ij}S_{ij}$ at 256^3 (left), 512^3 (center), and 1024^3 (right) grid resolutions

tube-like region (see scale numbers 3 and 4 in Figure 5.10), highly stretched particularly for the smaller scales; the transition to sheet-like structures appears to be significant at scale number 4 and becomes obvious at scale number 5, for which dominant structures span across almost all values of $\hat{C}$. On the other hand, $S_{ij}S_{ij}$ structures concentrate less in the tube-like region (see Figure 5.8 and compare scale numbers 3 and 4 of $S_{ij}S_{ij}$ in Figure 5.10 with those of $\omega_i\omega_i$ in Figure 5.12), while they show, at all intermediate scales, many more structures with smaller values of $\hat{C}$, characteristic of sheet-like geometries. The transition to sheet-like structures begins earlier, at scale number 3, for $S_{ij}S_{ij}$ than for $\omega_i\omega_i$, and is completed by scale number 5.

5.4 Effect of grid resolution in the geometry of structures

From Figures 5.7 and 5.8 it is observed that the 256^3 case does not capture well the dominance of sheet-like structures that occurs in both $\omega_i\omega_i$ and $S_{ij}S_{ij}$ in the small scales (scales numbers from 4 on). Figures 5.11 and 5.12 show, for $S_{ij}S_{ij}$, a tendency toward sheet-like structures at the smallest scale studied for the 256^3 case, although the smaller values of $\hat{C}$ present in the 512^3 and 1024^3 for the same scale number are not captured in the 256^3 case either. This is even more pronounced in the $\omega_i\omega_i$ field (see, in particular, Figure 5.10), for which the departure from tube-like region toward the sheet-like structures present at higher grid-resolutions is not obvious at all in the 256^3 case.

The 512^3 case performs better than the 256^3 case in describing the geometry of the structures at the scales of study, when each one is compared with its immediately higher grid resolution. For example, the visualization space at scale number 5, the smallest scale analyzed for 512^3, is rather similar to the 1024^3 case (see central and right columns of Figures 5.9–5.12), where structures with geometries transitioning from the tube-like region to the strongly sheet-like region are captured at both resolutions in more similar proportions. The 1024^3 case still shows a higher concentration of sheet-like structures, particularly for the $S_{ij}S_{ij}$ case.

These results are consistent with the observations of HF. They identified multiple modes of the stretched spiral vortex (Lundgren, 1982) in the numerical database and investigated their formation processes. They found that the highest grid resolution $k_{\max}\bar{\eta} \approx 4$ was needed to eliminate the

fragmentation of sheets for a precise capture of the spiral turns (sheet-like) of those structures and for a proper study of the dissipation field. Schumacher et al. (2005) found also the necessity of resolving sub-Kolmogorov scales when studying the very fine structures in scalar mixing, where sheets are also dominant in the scalar dissipation field. Sreenivasan (2004), based on intermittency arguments, proposed a revised grid resolution criterion, based on estimates of the ratio of maximum to average dissipation obtained from measured multi-fractal exponents (see Sreenivasan & Meneveau, 1988) much more stringent than the traditional $k_{\max}\bar{\eta} \approx 1$ criterion.

As previously noted, the largest and smallest scales for each grid resolution were left out of the analysis. The largest scale is dependent on boundary conditions and forcing applied and, therefore, of less interest in this particular study. The smallest scale was not analyzed to avoid interference with the iso-contouring step due to grid resolution effects. But three grid resolutions of the same flow realization provide the opportunity to verify whether that last statement holds. For that reason, Figures 5.9 to 5.12, include, for the 256^3 case (left column), one additional visualization space corresponding to scale number 5 (framed in a dashed-line box). When compared to the homologous scale number for the higher grid resolutions, it can be seen that the strong sheet-like character of the structures is not well captured in the 256^3. A possible explanation is that sheet-like structures at that resolution are more fragmented into smaller structures (part of the original ones). Some will still be sheet-like but their tube-like area coverage increases since the nearly planar area is reduced and the surface is still closed, which results in higher values of $\hat{C}$ directly affecting their location in the visualization space. Some others can even result in small blob-like structures or, in general, rather distinct geometries than the original sheets of which they are fragments. This is confirmed when the population of individual structures at that scale number is evaluated, since there is a high increase of small-area structures. The pixelization effect seen in Figure 5.6 for the two-dimensional plane cuts, when extended to three-dimensions (where the iso-contours, and thus the individual structures, are obtained) can help to visualize the scenario described above.

5.5 Clustering results for the 1024^3 case

As part of the classification step of the methodology, clustering techniques are applied to the structures obtained from all merged scales under study. This is done independently for structures of $\omega_i\omega_i$ and $S_{ij}S_{ij}$. Only the 1024^3 database is considered here. The number of structures present at each scale largely increases with the scale number (i.e., for smaller and smaller scales). Therefore, geometries of structures of larger scales could be under-represented in the clustering process. To avoid that situation a stratified random sampling with a disproportionate allocation, based on the standard deviation of the population of each scale number, is applied among the present scales prior to the clustering algorithm. See Appendix H for more details.

The results of the clustering algorithm applied individually to $\omega_i\omega_i$ and $S_{ij}S_{ij}$ structures are presented in Figure 5.13. An optimum number of 3 clusters was automatically obtained by the algorithm for $\omega_i\omega_i$, while the structures of $S_{ij}S_{ij}$ were optimally clustered in 2 groups. Optimality scores obtained during the automatic determination of the number of clusters for $\omega_i\omega_i$ (left) and $S_{ij}S_{ij}$ (right) are plotted in Figure 5.14. The optimality score is computed as the mean value of the silhouette coefficient of all the clustered elements minus the standard deviation of those silhouette coefficients. Higher mean values of the silhouette coefficient imply that the elements were clustered in groups where they have a high degree of membership. Small values of the standard deviation of the silhouette coefficients indicate homogeneity in that level of membership among the clustered elements. The combination of a high mean and a low standard deviation is sought for an optimum clustering result. We note that the optimality scores obtained are rather low (less than 0.5, 1 being the maximum achievable), even for the optimum number of clusters. Also, the optimality score associated with the optimum number of clusters determined for each case does not differ significantly from the rest. These two facts are an indication that the elements to cluster are organized as a cloud of points continuously distributed throughout the feature space of parameters used for clustering, instead of being organized in well distinguishable groups that would result in higher optimality scores and more variation among those scores for non-optimal number of clusters. A projection of that feature space is the visualization space where the results have been plotted,

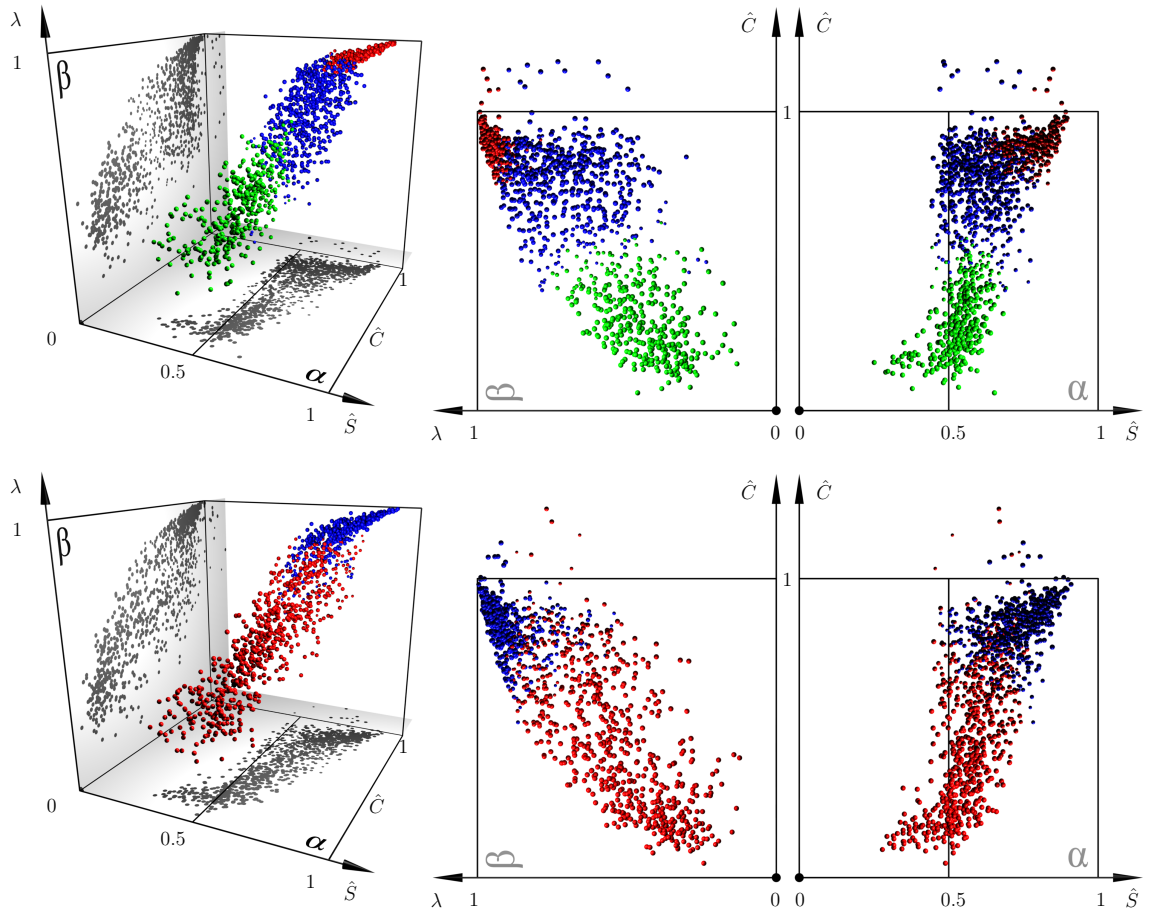

Figure 5.13: Clustering results in the visualization space—3D view (left) and lateral (center) and top (right) projections—with glyphs (spheres) representing the optimum clusters of structures educed from the stratified random sample with optimum allocation of the sets of $\omega_i\omega_i$ (top) and $S_{ij}S_{ij}$ (bottom) structures. Glyphs are scaled by the normalized value of the silhouette coefficient, which indicates the degree of membership of that element to the assigned cluster

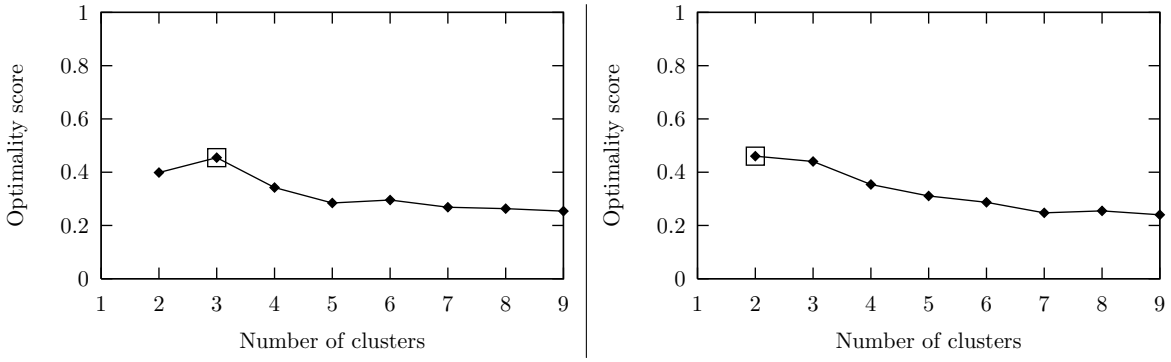

Figure 5.14: Optimality scores for different number of clusters obtained during the application of the clustering algorithm to the set of structures of $\omega_i\omega_i$ (left) and $S_{ij}S_{ij}$ (right) independently. Optimum number of clusters (square point) of 3 and 2 were automatically determined for $\omega_i\omega_i$ and $S_{ij}S_{ij}$, respectively

where it is possible to see also the continuously distributed cloud of glyphs.

5.6 Discussion

The dominance of tube-like structures at intermediate scales of $\omega_i\omega_i$ is consistent with the presence of so-called 'worms' reported in the fluid mechanics literature (see, for example, Siggia, 1981; Jiménez et al., 1993). Tube-like structures appear also at intermediate scales of $S_{ij}S_{ij}$ but in less proportion than for $\omega_i\omega_i$. At all scales analyzed, $S_{ij}S_{ij}$ shows, on average, more planar geometries than $\omega_i\omega_i$. Also the transition to sheet-like structures occurs earlier (larger scale) for $S_{ij}S_{ij}$.

The maximum departure between the spectra of $\omega_i\omega_i$ and $S_{ij}S_{ij}$ occurs at the intermediate scales (scale numbers 3 and 4), as observed in Figure 5.3. This seems to translate into differences in the geometrical character of structures of $\omega_i\omega_i$ and $S_{ij}S_{ij}$ at those scales numbers. In physical space, the higher concentration of tube-like structures found in the enstrophy field might be one geometrical link to its higher intermittency, when compared to the dissipation field.

At the smallest scale, both fields show a clear dominance of sheet-like structures. They appear highly stretched, that is, with small thickness, but their spatial extent can be significant. Instabilities of vortex sheets have been suggested as a primary mechanism responsible for the generation of vortex tubes in turbulent flows. Vincent & Meneguzzi (1994) found that the production of vortex sheets and their subsequent roll-up, forming tubes, shows a strong correlation between scales, and occurs in a one-step process (in contrast with Richardson multi-step cascade picture). Furthermore, they explain the alignment of vorticity with the intermediate strain-rate eigenvector as a consequence of vorticity sheet production by strong strain, instead of tube formation. HF identified the stretched spiral vortex (Lundgren, 1982) in homogeneous isotropic turbulence, appearing in three modes (two symmetric and one antisymmetric), that involve one or multiple vortex sheets interacting to generate tubes. While the stretched spiral vortex was not found in the work of Vincent & Meneguzzi (1994), that was attributed by HF to the increased grid resolution required to avoid fragmentation of the spiral turns. The correlation of geometries for $\omega_i\omega_i$ and $S_{ij}S_{ij}$ at the smallest scale is consistent with the known feature of sheets, in which strain and rotation rates are both large and correlated

(Ruetsch & Maxey, 1992; Horiuti & Takagi, 2005).

Previous studies of the enstrophy field also suggest (see Nomura & Post, 1998, and the references therein) that its geometry depends on its local magnitude: intense regions appear tube-like while moderate enstrophy regions seem to be more sheet-like. These considerations are, nevertheless, independent of the scale. Besides the iso-contour value of the mean plus twice the standard deviation of each filtered component field, whose results have been presented here, we examined also the mean plus three times the standard deviation, with no significant differences of the geometries educed for each field. A wider range of iso-contour values would help clarify the sensitivity of the geometries Nonetheless, we note that the categorization of globally intense or moderate values of the original field (containing all scales) based on the iso-contour value is not directly applicable to its component fields after the multi-scale decomposition.

The 256^3 grid resolution ($k_{\max}\bar{\eta} \approx 1$) was unable to reproduce the predominance of highly stretched sheet-like structures found for the smaller scales at higher grid resolutions. This indicates that sub-Kolmogorov scales must be resolved for a proper geometrical study of the smallest structures in turbulence, as has been suggested in the literature (see Shumacher & Sreenivasan, 2005; Horiuti & Fujisawa, 2008) when studying intermittent fields: their high fluctuations (manifested in the long tails of the volume pdfs in physical space) will occur at very fine scales. These, in general, can be substantially smaller than the average Kolmogorov length scale, $\bar{\eta} = \left(\nu^3/\langle\epsilon\rangle\right)^{1/4}$, defined in terms of the average rate of kinetic energy dissipation per unit mass, $\langle\epsilon\rangle$, and the viscosity of the fluid, ν, and traditionally used to define the largest dynamically significant wavenumber resolved in DNS, $k_{\max}$, such that $k_{\max}\bar{\eta} \approx 1$. As noted in §5.2 the volume pdfs of the different scale component fields obtained from $\omega_i\omega_i$ and $S_{ij}S_{ij}$ show wider ranges for smaller scales, indicating that higher fluctuations of those two fields occur in the small scales and confirming the intermittency of those two fields.